Inorganic Chemistry

Elucidation of the Off-Center Displaced Mo in Octahedral Coordination in Ba_2MoO_5

Andries van Hattem, Laurent de Geus, Ana Sacristán, Robert Dankelman, Sebastian Couweleers, Christoph Hennig, Jean-Christophe Griveau, Eric Colineau, Kathy Dardenne, Jörg Rothe, Tim Pruessmann, Rudy J. M. Konings, and Anna L. Smith*

Cite This: https://doi.org/10.1021/acs.inorgchem.4c03617

Read Online

ACCESS | Metrics & More | Article Recommendations | Supporting Information

ABSTRACT: The detailed crystal structure as well as the heat capacity at low temperature and standard entropy of Ba_2MoO_5 are reported for the first time. High-resolution X-ray and neutron diffraction were employed to reveal the structural features of this compound. Ba_2MoO_5 has a six-coordinated Mo and a strongly negative excess volume with respect to the binary oxides. X-ray absorption near edge structure (XANES) spectroscopy at the Mo K-edge shows Mo to be in the oxidation state 6+. The pre-edge peak in the XANES spectrum indicates a distorted octahedral environment, in line with the results from diffraction studies and FDMNES calculations. The standard entropy and heat capacity of Ba_2MoO_5 at 298.15 K, determined with a thermal-relaxation technique, are calculated to be respectively 223.2 ± 7 and 184.7 ± 5 $J \cdot K^{-1} \cdot mol^{-1}$. The obtained thermodynamic properties are discussed in the context of the literature reports on molybdate compounds.

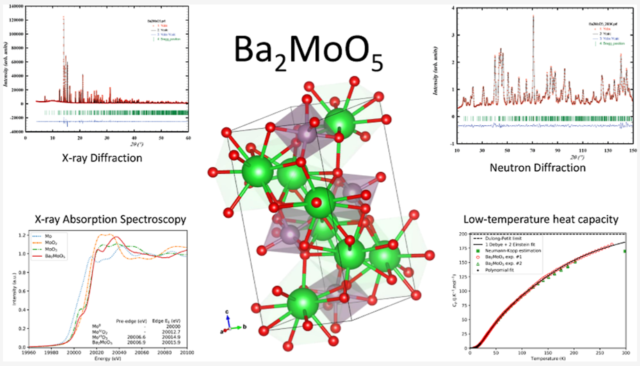

INTRODUCTION

Molybdates are a group of compounds with interesting properties in the energy field, for applications in and relevance for catalysis,[1,2] batteries[3] and nuclear safety,[4] because Mo is a high-yield fission product. Besides, molybdates got attention in the field of luminescence as phosphor host materials.[5,6] Molybdates cannot be considered a uniform group because the structural differences in the molybdate oxyanion are substantial as both tetrahedral and octahedral coordination have been reported in literature. In addition, the arrangement of the polyhedra can range from isolated to corner-, edge- or face-sharing. These different coordination environments will strongly affect the characteristics and properties of the compounds. A striking example are the M_2MoO_5 compounds that we encountered in our studies of the $MO\text{-}MoO_3$ phase diagram (M = Ba,Pb).[4,7] Pb_2MoO_5 forms a framework of Pb—O9 and Mo—O4 polyhedra, whereas Ba_2MoO_5 is stated to be orthorhombic with octahedral Mo coordination and isostructural with $K_2VO_2F_3$ by ref 8 based on private communication with Negas and Roth. The compound Ba_2MoO_5 has been mentioned in the literature several times in the 1970s.[8−10] However, no detailed structural investigation of the atomic positions has been reported, except for a recent reinterpretation of the data reported in ref 8 by Zavodyannyi.[11]

The atomic structures of two tungstate compounds with divalent cations Sr_2WO_5 and Ba_2WO_5 that are seemingly isostructural with our title compound Ba_2MoO_5 were recently found to differ. In comparison to earlier studies, a more physical description of the atomic displacement parameters of Sr_2WO_5 was obtained in space group $Pna2_1$ instead of $Pnma$. The Sr_2WO_5 structure exhibits corner-sharing distorted WO_6 octahedra that form infinite tilted zigzag chains, while Ba_2WO_5 has no tilt in the zigzag chain of octahedra.[12] This raises the question of how the molybdate analog Ba_2MoO_5 crystallizes exactly.

In this article, we investigate Ba_2MoO_5 using X-ray and neutron-based techniques to solve the open questions on its crystal structure. Moreover, the heat capacity of the compound has been measured at low temperatures, yielding the heat capacity and standard entropy at 298.15 K for the first time.

EXPERIMENTAL SECTION

Synthesis. To synthesize Ba_2MoO_5, $BaCO_3$ (99%, Fluka) and MoO_3 (99.5%, Alfa Aesar) were thoroughly mixed in a 2:1 molar ratio. The mixture was heated 3 times in an alumina crucible under Ar

Received: August 26, 2024
Revised: December 13, 2024
Accepted: December 19, 2024

atmosphere at 1173 K for a total time of about 70 h with intermittent regrinding. Since the compound attracts moisture from the air in minutes, it was handled and stored in an Ar-filled dry glovebox with H_2O and O_2 contents maintained below 5 ppm.

X-ray and Neutron Diffraction. High resolution synchrotron XRD (sXRD) measurements were collected using the XRD-1 station at the ROBL beamline (BM20) at ESRF.[13,14] This station is equipped with a 6-circle diffractometer and a Eiger CdTe 500k detector (Dectris). The wavelength of the synchrotron radiation was set to λ = 0.774901 Å. The beam size was 300 × 300 μ m^2. The sample holder used in the measurements was a 300 μm diameter glass capillary closed with Epoxy glue itself enclosed inside a Kapton tube. Data were collected in transmission mode at 296 K and reduced using the PyFAI software suite.[15]

Neutron diffraction (ND) on Ba_2MoO_5 was performed at the PEARL beamline at the Hoger Onderwijs Reactor (HOR) at TU Delft.[16] The sample was loaded in a vanadium Null-alloy container hermetically closed with a rubber O-ring. A fixed wavelength of 1.667 Å in the angle range $11 \leq 2\theta \leq 159°$ was used. Data were collected at 293 K.

The diffraction patterns were analyzed using the Rietveld profile refinement method[17,18] in the FullProf suite.[19] Structural visualization was done using the VESTA software.[20]

X-ray Absorption Near Edge Spectroscopy. X-ray absorption near edge spectroscopy at the Mo K-edge (20 keV) was performed at the INE Beamline[21] of the KIT Light Source (Karlsruhe, Germany), which has an energy of 2.5 GeV and a maximum current of 170 mA as operating conditions in the KARA storage ring. A Ge(422) double-crystal monochromator was used and the beam spot size of 500 μm by 500 μm was obtained using Rh-coated mirrors. The Ba_2MoO_5 sample, as well as MoO_2 and MoO_3 references were diluted in BN powder and pressed into pellets for the measurements, enclosed inside a Kapton foil.

XANES spectra were collected at room temperature in fluorescence mode, using a combination of two silicon drift detectors, viz. a Vortex-ME4 (4 elements) and a Vortex-60EX (1 element, Hitachi/SIINT). A step size of 0.75 eV was used in the edge region. The energy E_0 of the edge absorption threshold position was taken at the inflection point of the spectrum. The position of the prepeak was selected from the recorded maximum before the edge. Several acquisitions were performed on the same sample and summed up to improve the signal-to-noise ratio. Before averaging the scans, each spectrum was aligned using the XANES spectrum of a metallic molybdenum reference foil measured in transmission between the second and third ionization chambers. The ATHENA[22] software was used to analyze the data. The inflection point is taken as the absorption edge position, while the prepeak (when present) was characterized using its peak maximum.

XANES spectra of Ba_2MoO_5, $BaMoO_4$ and $BaMoO_3$ have been calculated with the FDMNES code[23,24] using the sXRD based Ba_2MoO_5 structure presented in this work and previously published structures for $BaMoO_4$ and $BaMoO_3$.[4] The calculations were performed with a cluster radius of 7 Å using self-consistent field (SCF) and the PBE96 exchange−correlation potential. The calculated spectra were normalized and the maxima of the whitelines (WL) were aligned to the experimental spectrum of Ba_2MoO_5 for better comparability.

Low-Temperature Heat Capacity. The low-temperature heat capacity of Ba_2MoO_5 was measured on pressed pellets of 3 mm diameter with a Quantum Design PPMS 9T machine at JRC Karlsruhe. The heat capacity of the sample equals the difference between the total measured heat capacity and the addenda curve. A pellet of 11.50(10) mg (exp. #1) was encapsulated in 0.824(5) mg Stycast to prevent moisture uptake and improve the thermal heat transfer to the sample platform.[25] The Stycast contribution as well as the addenda curve were subtracted from the measured heat capacity to obtain the heat capacity of the Ba_2MoO_5 material itself. The temperature domain is 7.1−277.2 K.

For the data analysis, two fits were used. Toward the lower limit (T < 20 K), the lattice contribution to the heat capacity was fitted to a polynomial expression

$$C_p(T) = \sum_{n=3,5,7,9} B_n T^n \tag{1}$$

where B_n is a constant and T is the temperature in K. A linear combination of n_D times a Debye function ($D(\Theta_D, T)$) and $n_{E1} + n_{E2}$ times an Einstein function ($E(\Theta_{Ei},T)$) was used to fit the data at higher temperatures (T > 20 K). The formula used for fitting in this work reads thus

$$C_v(T) = n_D \cdot D(\Theta_D, T) + \sum_{i=1,2} n_{E_i} \cdot E(\Theta_{E_i}, T) \tag{2}$$

where the formulas for the Debye (with $x = \Theta_D/T$) and Einstein functions are

$$D(\Theta_D, T) = 9R\left(\frac{\Theta_D}{T}\right)^3 \int_0^{\Theta_D/T} \frac{e^x x^4}{(e^x - 1)^2} dx \tag{3}$$

and

$$E(\Theta_E, T) = 3R\left(\frac{\Theta_E}{T}\right)^2 \frac{e^{\Theta_E/T}}{(e^{\theta_E/T} - 1)^2} \tag{4}$$

The classical Dulong−Petit limit ($C_v = 3nR$) is hidden in the sum of $n_D + n_{E1} + n_{E2}$, while $C_p \approx C_v$ in the fitted temperature range. The standard entropy at 298.15 K was then calculated by integration of the fits in the temperature domain 0−298.15 K. The total uncertainty in the measured heat capacity is estimated to be at maximum 3%. The uncertainty on the heat capacity was used in the uncertainty determination on the standard entropy.

For verification, the heat capacity of a pellet of Ba_2MoO_5 encapsulated in Stycast was also measured on a Quantum Design Versalab machine at TU Delft in the temperature window 50−202 K (exp. #2). The mass of this pellet is 10.40(10) mg with 0.930(10) mg Stycast.

■ RESULTS AND DISCUSSION

X-ray and Neutron Diffraction. A yellow powder was obtained from the above-mentioned synthesis. As a starting point for profile refinement, the atomic positions of $K_2VO_2F_3$ were used, as has been suggested by Ryan et al.[8,10] The refinement of the synchrotron X-ray and neutron diffraction data in space group *Pnma* (62) were successful, as can be seen in Figures 1 and 2. In the synchrotron X-ray diffraction pattern, a few minor unexplained peaks (I/I_{max} < 0.4%) were found at 2θ = 11.4, 12.4, 13.2 and 22.4°. No clear attribution to these peaks can be given, but these may be reaction products of moisture attraction.

The cell parameters as obtained from the refinements are given in Table 1 and compared with values from literature that are obtained by XRD. The cell parameters are in line with literature and each other, though not always within the reported errors. The atomic positions refined from neutron and synchrotron X-ray diffraction are given in Tables 2 and 3, respectively. The isotropic atomic displacement parameters are optimized as well. The values are given in Table 2 for the synchrotron X-ray diffraction data and in Table 3 for the neutron diffraction data.

It is interesting to note that the structure of Ba_2MoO_5 is closely related to arcanite (K_2SO_4), which is adopted by Cs_2MoO_4 while a related monoclinic structure is adopted by K_2MoO_4.[27] The "additional" oxygen in the structure promotes an octahedral coordination of Mo compared to the tetrahedral coordination in Cs_2MoO_4, without affecting the unit cell

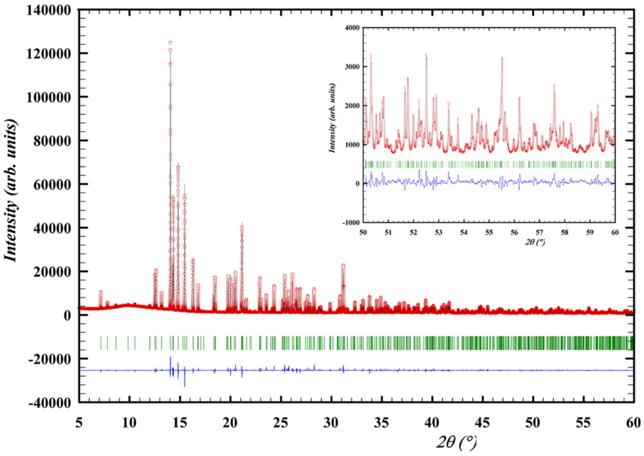

Figure 1. Experimental (Y_{obs}, in red) and calculated (Y_{calc}, in black) sXRD patterns of Ba_2MoO_5 at ambient temperature. The difference between calculated and experimental intensities $Y_{obs} - Y_{calc}$ is shown in blue. The angular positions of Bragg reflections are shown in green. Measurement at $\lambda = 0.774901$ Å.

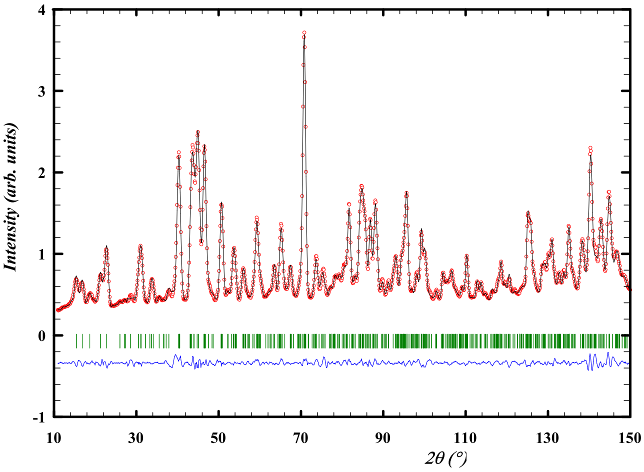

Figure 2. Experimental (Y_{obs}, in red) and calculated (Y_{calc}, in black) ND patterns of Ba_2MoO_5 at ambient temperature. The difference between calculated and experimental intensities $Y_{obs} - Y_{calc}$ is shown in blue. The angular positions of Bragg reflections are shown in green. Measurement at $\lambda = 1.667$ Å.

Table 1. Refined Cell Parameters of Ba_2MoO_5 Based on sXRD and ND in Space Group *Pnma* (62) ($\alpha = \beta = \gamma = 90°$) in This Work Compared with Literature. sXRD and ND are Synchrotron X-ray Diffraction and Neutron Diffraction, Respectively

method	*a* (Å)	*b* (Å)	*c* (Å)	*V* (Å^3)
sXRD (this work)	7.41082(10)	5.76170(10)	11.38820(10)	486.26
ND (this work)	7.4009(18)	5.7534(14)	11.3682(19)	484.06
XRD[8]	7.4097(7)	5.7603(6)	11.3096(8)	482.72
XRD[9]	7.412(1)	5.769(1)	11.380(2)	486.61

Table 2. Refined Atomic Positions of Ba_2MoO_5 and Isotropic Atomic Displacement Parameters Based on Synchrotron X-ray Diffraction[a]

site	Wyckoff	*x*/*a*	*y*/*b*	*z*/*c*	*B* (Å^2)
Ba1	4c	0.47913(4)	0.25	0.71144(3)	0.371(7)
Ba2	4c	0.18429(5)	0.25	0.41632(3)	0.42(8)
Mo	4c	0.18383(8)	0.25	0.06868(4)	0.228(10)
O1	4c	0.2790(5)	0.25	0.9082(4)	1.18(10)
O2	8d	0.3202(4)	0.0078(4)	0.1186(19)	0.36(5)
O3	4c	0.0211(5)	0.25	0.1906(3)	2.00(10)
O4	4a	0	0	0	0.39(8)

[a] $R_p = 13.4$, $R_{wp} = 13.8$, $R_{exp} = 4.83$, $\chi^2 = 8.22$.

Table 3. Refined Atomic Positions and Isotropic Atomic Displacement Parameters of Ba_2MoO_5 Based on Neutron Diffraction[a]

site	Wyckoff	*x*/*a*	*y*/*b*	*z*/*c*	*B* (Å^2)
Ba1	4c	0.477(4)	0.25	0.71255(3)	0.64(6)
Ba2	4c	0.1865(4)	0.25	0.41604(3)	0.64(5)
Mo	4c	0.1839(3)	0.25	0.07172(2)	0.39(3)
O1	4c	0.2816(4)	0.25	0.91176(3)	0.89(5)
O2	8d	0.3244(2)	0.0086(4)	0.11755(14)	1.21(3)
O3	4c	0.0254(4)	0.25	0.1952(3)	1.28(6)
O4	4a	0	0	0	0.94(4)

[a] $R_p = 5.7$, $R_{wp} = 6.43$, $R_{exp} = 1.38$, $\chi^2 = 21.6$.

Table 4. Bond Lengths for Ba_2MoO_5 Obtained From Synchrotron X-ray and Neutron Diffraction Data via Rietveld Refinement[a]

	synchrotron X-ray diffraction			
bond	Av. (Å)	Min (Å)	Max (Å)	S.R. (Å)
Ba1−O	2.82	2.607(4)	2.8906(3)	2.92
Ba2−O	2.89	2.741(3)	3.064(3)	2.92
Mo−O1	1.959(5)			1.99
Mo−O2(x2)	1.814(3)			1.99
Mo−O3	1.839(4)			1.99
Mo−O4(x2)	2.1313(5)			1.99
	neutron diffraction			
bond	Av. (Å)	Min (Å)	Max (Å)	S.R. (Å)
Ba1−O	2.83	2.660(5)	2.892(4)	2.92
Ba2−O	2.87	2.733(4)	3.042(4)	2.92
Mo−O1	1.956(2)			1.99
Mo−O2(x2)	1.812(3)			1.99
Mo−O3	1.830(4)			1.99
Mo−O4(x2)	2.1414(17)			1.99

[a] Effective ionic radii for the column "S.R." are taken from Shannon.[26]

volume as the unit cell volumes of Cs_2MoO_4, K_2MoO_4 and Ba_2MoO_5 follow a linear trend as a function of the ionic radius of the (earth-)alkaline cation.

The refined distances in the various polyhedra are summarized in Table 4 and compared to the sum of the Shannon radii of the ions.[26] The effective ionic radii as reported by Shannon and used here are Ba^{2+}(X) = 1.52 Å and Mo^{6+}(VI) = 0.59 Å. The oxygen coordination is V (O1, O2 and O3) and VI (O4), the Shannon radii being 1.38 and 1.40 Å for IV- and VI-coordination, respectively. The two Ba-polyhedra are coordinated to 10 O anions and have six different Ba−O bond lengths, ranging from 2.607(4) Å to 2.8906(3) Å (sXRD) or 2.660(5) Å to 2.892(4) Å (ND) for Ba1−O, which is short in comparison with the sum of ionic radii, and from 2.741(3) Å to 3.064(3) Å (sXRD) or 2.733(4) Å to 3.042(4) Å (ND) for Ba2−O, which is on average close to the sum of Shannon ionic radii.

The Mo-octahedra have a slightly off-centered Mo-atom, see Figure 3 and the detailed zoom in Figure 4. The Mo-octahedra

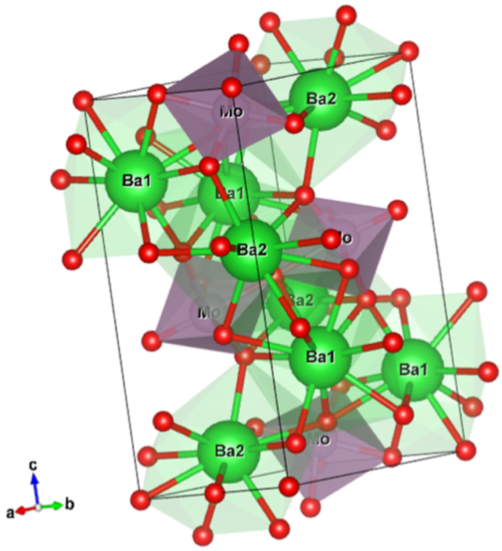

Figure 3. 3-Dimensional view of the crystal structure of Ba_2MoO_5. The chains of Mo-octahedra can be seen, as well as the off-center Mo-atom. The green, purple and red atoms are Ba, Mo and O, respectively.

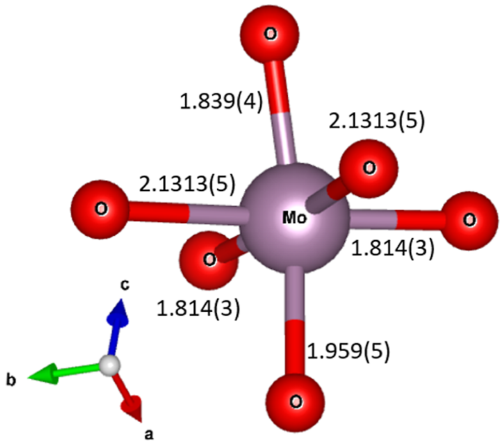

Figure 4. Detailed view of the coordination of Mo showing the off-center Mo-atom and bond lenghts.

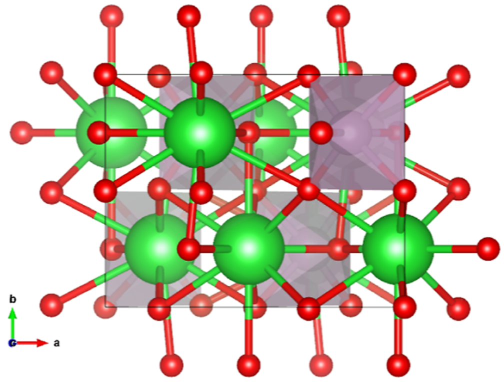

Figure 5. View of the crystal structure of Ba_2MoO_5 along the *c*-axis, showing the Mo-octahedra are aligned from this perspective. The green, purple and red atoms are Ba, Mo and O, respectively.

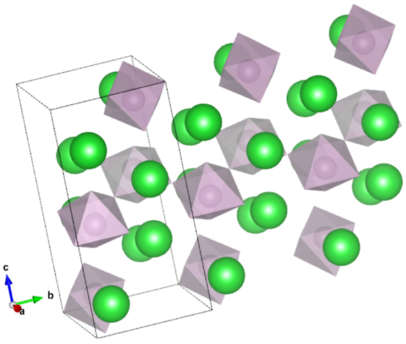

Figure 6. View of the crystal structure of Ba_2MoO_5, showing the corner-sharing Mo-octahedra.

are corner-sharing via the O4 ions. The Mo−O4−Mo angle equals 180° by symmetry and the chain is thus developing in the *b*-direction in a zigzag mode with nontilted octahedra and with rather long Mo−O4 distances of 2.1313(5) Å (sXRD) or 2.1414(17) Å (ND). The nontilted zigzag alignment can be seen from the top in Figure 5 and the chains are better visible in the three-dimensional perspective in Figure 6. Bond angles are visualized in Figure S.1 and tabulated in Table S.1.

The average Mo−O bond length, 1.9482 Å (sXRD) or 1.9486 Å (ND), is close to but somewhat lower than the sum of Shannon ionic radii (1.97−1.99 Å depending on coordination). Furthermore, it is larger than the Mo−O bond length in undistorted Mo−O6 octahedra (1.92 Å) as derived by Shannon, and thus indicates a distortion.[26] Instead of using only the tabulated values for Mo^{6+}(VI) and O^{2-}, the equation by Shannon[26] for the relation between distortion of the octahedron Δand the average Mo^{6+}−O bond length $\bar{R}$ using the mean-square relative deviation from the average[28] reads

$$\bar{R} = 1.920 + 3.73\Delta \tag{5}$$

with[28]

$$\Delta = \frac{1}{6}\sum_{i=1}^{6}\frac{(R_i - \bar{R})^2}{\bar{R}^2} \tag{6}$$

Calculation of $\bar{R}$ using the distortion parameter Δ based on the bond lengths R_i obtained in this work using sXRD and ND yields $\bar{R}$ = 1.94 Å in both cases, showing that the structure of Ba_2MoO_5 fits very well the general trend.

The molar volume derived from the crystallographic density of Ba_2MoO_5 is lower than the stoichiometric sum of the molar volumes of the constituting oxides. This is different from other known molybdate compounds, as is shown in Table S.2. $CoMoO_4$, $FeMoO_4$ and $NiMoO_4$, in which Mo is octahedrally coordinated like in Ba_2MoO_5, have a strongly positive excess volume (>5%) due to the open arrangement of the MoO_6 and AO_6 octahedra with a large fraction of corner sharing. The excess volume of the tetrahedrally coordinated arcanite-type alkali molybdates, to which the structure of Ba_2MoO_5 is related, is strongly positive (>5%), resulting from a loose arrangement of edge and corner sharing polyhedra. The excess volume of $AMoO_4$ molybdate scheelite compounds (A = Ca, Sr, Ba, Pb) varies from slightly negative (−1%) to strongly positive (>5%), in an open arrangement with corner-sharing MoO_4 tetrahedra. In Pb_2MoO_5, the corner-sharing of the polyhedra results in a very open structural arrangement as well. This means that Ba_2MoO_5 (and the isostructural Ba_2WO_5) is an exceptional case regarding its strongly negative excess volume, resulting from the very effective spatial ordering/

packing of the polyhedra in the structure through face sharing made possible by the octahedral coordination of Mo, as can also be seen in Figure S.2.

Recently, Jantz et al.[12] showed that the compounds Sr_2WO_5 and Ba_2WO_5 have a different ordering of Mo-octahedra. Sr_2WO_5, previously also refined in space group *Pnma* (62), can be more adequately refined in space group $Pna2_1$ (33), while the earlier assignment of Ba_2WO_5 in space group *Pnma* was shown to be accurate. On the atomic level, however, this new description of Sr_2WO_5 yielded another view on the atomic displacement parameters. The connection between the W-octahedra is different: for Sr_2WO_5 infinite tilted chains were found, while Ba_2WO_5 has nontilted chains of octahedra. Herein, an attempt to refine the diffraction data in space group $Pna2_1$ did not yield an improved refinement when judged from statistical significance; the Mo-octahedra form chains in both space groups. From a principal point of view, no distinction can be made between the space groups *Pnma* (62) and $Pna2_1$ (33) or, after exchanging the lattice parameters for consistency, $Pn2_1a$. There are several reasons to prefer space group *Pnma*, however: the consistency with existing literature on Ba_2MoO_5,[8−11] the similarity to Ba_2WO_5,[12] the fact that the solution in *Pnma* has less parameters to adjust and only positive atomic displacement parameters (see Tables S.3 and S.4). Thus, Ba_2MoO_5 and Ba_2WO_5 are structurally similar and both have a strongly negative excess volume.

X-ray Absorption Near Edge Spectroscopy. The oxidation state of Mo in Ba_2MoO_5 was determined using X-ray absorption near edge structure spectroscopy. In Figure 7, the collected XANES spectra around the Mo K-edge are shown for Ba_2MoO_5 together with the reference materials Mo, MoO_2 and α-MoO_3. The derived absorption edge and pre-edge peak features are tabulated in Figure 7 as well. Ba_2MoO_5 exhibits an energy shift with respect to Mo-metal and MoO_2 and the E_0 is very close to that of α-MoO_3, indicating an oxidation state of 6+.

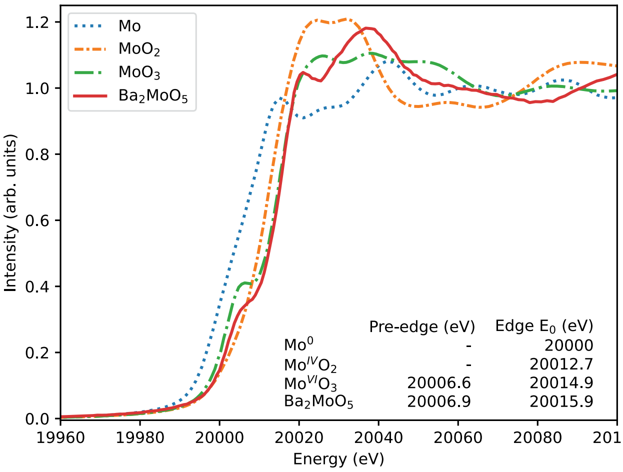

Figure 7. X-ray absorption near edge structure spectra of Ba_2MoO_5 measured at the Mo K-edge with reference materials Mo^0-metal, $Mo^{IV}O_2$ and α-$Mo^{VI}O_3$. The uncertainty on the determined edges is ±1 eV.

The pre-edge peak in both 3d and 4d metals can give some insight into the geometry around the atom of which a core electron is excited. The transition moment from Mo(1s) to Mo(4d) is forbidden in the electric dipole approximation, but allowed in the electric quadrupole approximation. However, the intensity of a quadrupole transition is much lower than the intensity of an allowed electrical dipole transition, and the pre-edge peak intensity is to be ascribed to d−p orbital hybridization. Group theoretical considerations show that for O_h symmetry there will be no mixing, while for T_d symmetry there is. Moreover, distorted octahedral symmetry exhibits a pre-edge peak, but with a lower intensity than compounds with a tetrahedral arrangement.[29] Herein, for Ba_2MoO_5, a pre-edge peak is observed, but less intense than that of α-MoO_3, which has a distorted octahedral symmetry. In $PbMoO_4$,[30] $BaMoO_4$[4] and Pb_2MoO_5,[7] all having MoO_4^{2-}-tetrahedra, an intense pre-edge peak is visible, while for $BaMoO_3$,[4] which has undistorted octahedral symmetry around Mo, no pre-edge peak is visible. The pre-edge peak indicates clearly a distortion from octahedral symmetry around the Mo-site and the pre-edge peak found with XANES is thus consistent with the Mo-octahedron with off-center Mo as found using diffraction techniques.

The behavior of the pre-edge is moreover confirmed by the calculated XANES spectra of Ba_2MoO_5, $BaMoO_4$ and $BaMoO_3$, which are shown in Figure 8. Here $BaMoO_3$ is only showing a small shoulder, $BaMoO_4$ has a clear pre-edge peak and Ba_2MoO_5 is lying in the middle. Additionally, the calculated Ba_2MoO_5 spectrum is in good overall agreement with the experimental data, further validating the structural model of Ba_2MoO_5.

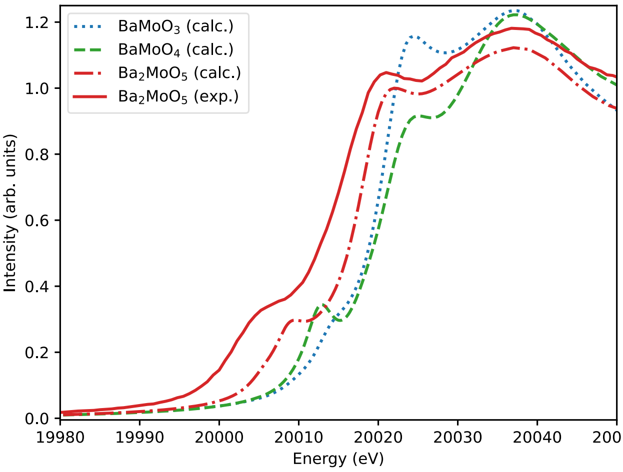

Figure 8. X-ray absorption near edge structure spectra as calculated (calc.) using FDMNES compared to the experimentally measured (exp.) spectrum of Ba_2MoO_5. The calculated spectra are aligned to the white line of Ba_2MoO_5 (exp.).

Heat Capacity and Standard Entropy. The low temperature heat capacity of Ba_2MoO_5 between 7.1 and 277.2 K is shown in Figure 9. No anomalies are observed in the studied temperature window and the results of the two measurements with different instruments are in good agreement. Mathematical fits as explained *supra* were made; the fitting parameters are given in Table 5. The relative difference between the fits and the experimental data is shown in Figure 10. Using the data below 10 K, the heat capacity in a plot of C_p/T vs T^2 yields a curve which extrapolates to 0, meaning there is no electronic contribution to the heat capacity and Ba_2MoO_5 is an insulating material (see also Figure S.3).

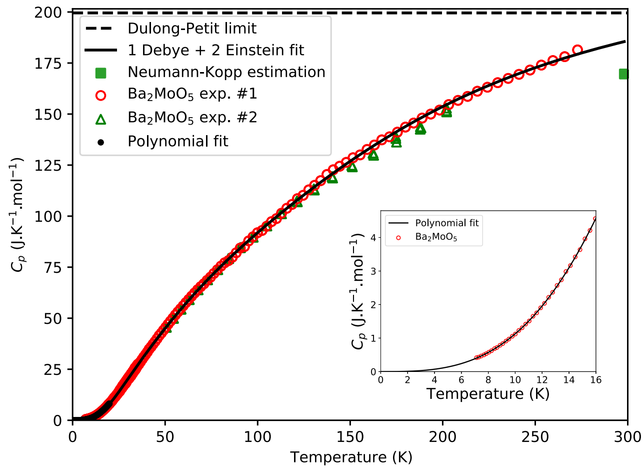

Figure 9. Heat capacity of Ba_2MoO_5 as measured in this work and fitted to a polynomial fit and a combined Debye−Einstein fit with comparison to the classical Dulong−Petit limit and Neumann−Kopp estimation. See the main text for the explanation of the fits.

Table 5. Fitting Parameters for the Low-Temperature Heat Capacity of Ba_2MoO_5

parameter	value
temp. range/K	7.1−20
B_3/mJ·mol^{-1}·K^{-4}	$1.096 \times 10^{-3} \pm 7 \times 10^{-5}$
B_5/mJ·mol^{-1}·K^{-6}	$4.509 \times 10^{-7} \pm 9 \times 10^{-7}$
B_7/mJ·mol^{-1}·K^{-8}	$-1.289 \times 10^{-9} \pm 4 \times 10^{-9}$
B_9/mJ·mol^{-1}·K^{-10}	$-6.253 \times 10^{-13} \pm 5 \times 10^{-12}$
temp. range/K	20−277.2
n_D/mol	2.71 ± 0.07
n_{E1}/mol	2.53 ± 0.10
n_{E2}/mol	3.88 ± 0.11
Θ_D/K	169.4 ± 2.1
Θ_{E1}/K	316.5 ± 11
Θ_{E2}/K	711.8 ± 17

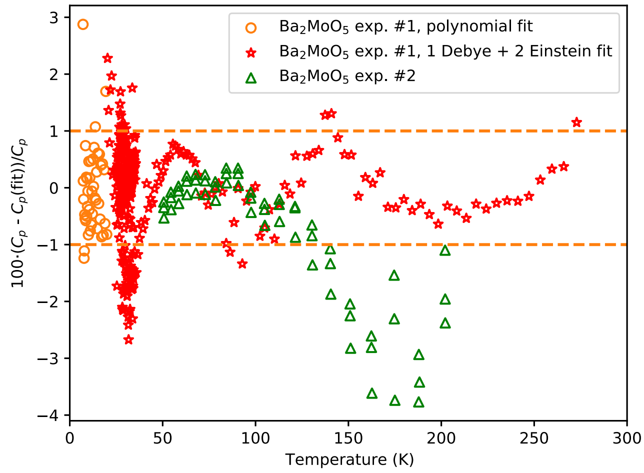

Figure 10. Relative difference between the experimental heat capacity data and the polynomial and combined Debye−Einstein fit. See the main text for the explanation of the fits.

In Figure 11, the shaded areas represent the contribution to the entropy of the polynomial fit and the combined Debye−Einstein fit in the fully shaded and dashed areas, respectively. The obtained standard entropy is S_m° (298.15 K, Ba_2MoO_5) = 223.2 ± 7 J·K^{-1}·mol^{-1}. The heat capacity obtained by extrapolation is C_p(298.15 K, Ba_2MoO_5) = 184.7 ± 5 J·K^{-1}·mol^{-1}.

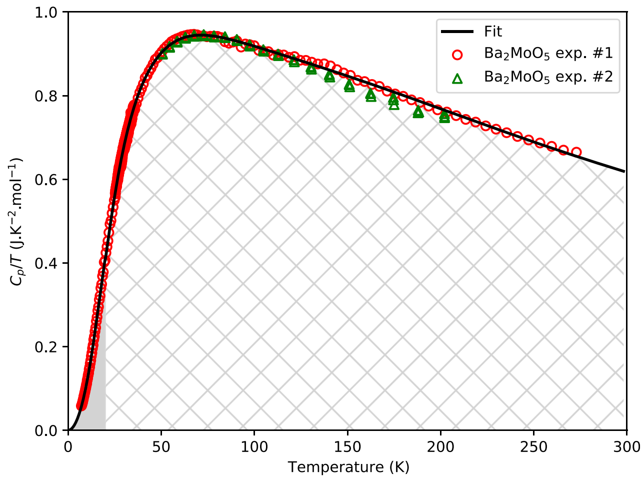

Figure 11. Heat capacity as plotted in C_p/T vs T. The shaded areas represent the contributions to the standard entropy as calculated using the two fits in their respective domains.

The obtained standard entropy value agrees very well with the value Smith et al.[4] optimized in a thermodynamic assessment of the Ba−Mo−O system, while the estimation method of Glaser[31] is quite far off. The heat capacity at 298.15 K is higher than the estimation of Smith et al., which was based on a Neumann−Kopp estimation[4] (Table 6).

Table 6. Comparison of the Standard Entropy and Heat Capacity at 298.15 K of Ba_2MoO_5 as Compared to an Estimation by Glasser[31] and an Optimization by Smith et al[4a]

parameter	value
S_m° (298.15 K) (this work)	223.2 ± 7
S_m° (298.15 K) (Calphad model[4])	223.7
S_m° (298.15 K) (estimation[31])	200.0
C_p (298.15 K) (this work)	184.7 ± 5
C_p (298.15 K) (Neumann−Kopp)	169.2

[a] All numbers in units of J·K^{-1} mol^{-1}.

The Neumann−Kopp approximation yields 169.2 J·K^{-1}·mol^{-1}, based on values for BaO (47.06 ± 0.1 J·K^{-1}·mol^{-1})[32] and α-MoO_3 (75.07 J·K^{-1}·mol^{-1}).[33] The failure of the Neumann−Kopp estimation for the heat capacity at 298.15 K can tentatively be explained by the fact that the heat capacity of layered α-MoO_3 is not yet approaching its Dulong−Petit limit ($C_v = 3nR$) at 298.15 K, unlike BaO and, as it turned out, the title compound Ba_2MoO_5. A check for $CaMoO_4$, $SrMoO_4$, $BaMoO_4$, $PbMoO_4$, $NiMoO_4$, $FeMoO_4$ and Pb_2MoO_5 showed that the difference to the Neumann−Kopp rule using α-MoO_3 is exceptionally large, as can be found in Table S.5. Moreover, all cases except Ba_2MoO_5 and Pb_2MoO_5 have a negative difference to the Neumann−Kopp rule (again, PbO is a layered compound that does not reach the Dulong−Petit limit at room temperature). Although the stoichiometry of Pb_2MoO_5 hints at a close relation with Ba_2MoO_5, the Mo-coordination in both compounds is different, which results in different lattice vibrations. To the best of our knowledge, no full low-temperature heat capacity of the compounds Ba_2WO_5 or Sr_2WO_5 or values at ambient temperature are available, making

https://doi.org/10.1021/acs.inorgchem.4c03617
Inorg. Chem. XXXX, XXX, XXX−XXX

a comparison to these compounds impossible. The comparatively high heat capacity for Ba_2MoO_5 asks thus for more investigation, either by measurements of the low-temperature heat capacity of Mo- or W-analogous compounds, or by complementary studies into the phonon behavior of Ba_2MoO_5 at room temperature and below using techniques such as Raman spectroscopy or inelastic neutron scattering.

■ CONCLUSIONS

Ba_2MoO_5 has been synthesized and structurally studied using neutron and X-ray diffraction. The compound was found to crystallize in space group *Pnma*. It has slightly distorted Mo-octahedra with off-center Mo that form corner-sharing nontilted zigzag chains. The pre-edge peak in the X-ray absorption spectrum indicates a distorted octahedral environment as well, while the oxidation state as determined using the absorption edge was found to be 6+. FDMNES calculations of the XANES spectrum further validated the structural model of Ba_2MoO_5. The standard entropy and heat capacity of Ba_2MoO_5 at 298.15 K were successfully determined. The obtained values are compared to available literature data for molybdate compounds and show that Ba_2MoO_5 is anomalous in terms of a strongly negative excess volume and strongly positive excess heat capacity, both relative to the binary oxides. It is tempting to attribute this to the peculiar arcanite K_2MoO_4-like structure in which the additional oxygen promotes the octahedral coordination of Mo compared to the tetrahedral coordination in arcanite, though achieved through a substantial deformation of the octahedra that includes off-center displacement of the Mo. The resulting face-sharing Ba- and Mo-polyhedrons build a dense structure.

■ ASSOCIATED CONTENT

Supporting Information

The Supporting Information is available free of charge at https://pubs.acs.org/doi/10.1021/acs.inorgchem.4c03617.

The data for the low-temperature heat capacity of Ba_2MoO_5 are attached as an Excel file (XLSX)

Supporting Information to "Elucidation of the Off-Center Displaced Mo in Octahedral Coordination in Ba_2MoO_5" (PDF)

Accession Codes

Deposition numbers 2377886–2377887 contain the supplementary crystallographic data for this paper. These data can be obtained free of charge via the joint Cambridge Crystallographic Data Centre (CCDC) and Fachinformationszentrum Karlsruhe Access Structures service.

■ AUTHOR INFORMATION

Corresponding Author

Anna L. Smith – *Radiation Science & Technology Department, Faculty of Applied Sciences, Delft University of Technology, Delft 2629JB, The Netherlands;* orcid.org/0000-0002-0355-5859; Email: a.l.smith@tudelft.nl

Authors

Andries van Hattem – *Radiation Science & Technology Department, Faculty of Applied Sciences, Delft University of Technology, Delft 2629JB, The Netherlands;* orcid.org/0000-0001-8814-4049

Laurent de Geus – *Radiation Science & Technology Department, Faculty of Applied Sciences, Delft University of Technology, Delft 2629JB, The Netherlands*

Ana Sacristán – *Radiation Science & Technology Department, Faculty of Applied Sciences, Delft University of Technology, Delft 2629JB, The Netherlands*

Robert Dankelman – *Radiation Science & Technology Department, Faculty of Applied Sciences, Delft University of Technology, Delft 2629JB, The Netherlands*

Sebastian Couweleers – *Radiation Science & Technology Department, Faculty of Applied Sciences, Delft University of Technology, Delft 2629JB, The Netherlands*

Christoph Hennig – *ESRF, the European Synchrotron, Grenoble Cedex 9 38043, France;* orcid.org/0000-0001-6393-2778

Jean-Christophe Griveau – *European Commission, Joint Research Centre, Karlsruhe D-76125, Germany*

Eric Colineau – *European Commission, Joint Research Centre, Karlsruhe D-76125, Germany*

Kathy Dardenne – *Institute for Nuclear Waste Disposal (INE), Radionuclide Speciation Department, Karlsruhe Institute of Technology (KIT), Eggenstein-Leopoldshafen 76344, Germany*

Jörg Rothe – *Institute for Nuclear Waste Disposal (INE), Radionuclide Speciation Department, Karlsruhe Institute of Technology (KIT), Eggenstein-Leopoldshafen 76344, Germany;* orcid.org/0000-0001-5366-2129

Tim Pruessmann – *Institute for Nuclear Waste Disposal (INE), Radionuclide Speciation Department, Karlsruhe Institute of Technology (KIT), Eggenstein-Leopoldshafen 76344, Germany;* orcid.org/0000-0002-7903-9199

Rudy J. M. Konings – *Radiation Science & Technology Department, Faculty of Applied Sciences, Delft University of Technology, Delft 2629JB, The Netherlands*

Complete contact information is available at: https://pubs.acs.org/10.1021/acs.inorgchem.4c03617

Notes

The authors declare no competing financial interest.

■ ACKNOWLEDGMENTS

This work has received funding from the Euratom research and training programme 2019–2020 through the research project PASCAL (Proof of Augmented Safety Conditions in Advanced Liquid-metal-cooled systems) under grant agreement no. 945341. We acknowledge the European Synchrotron Radiation Facility (ESRF) for provision of synchrotron X-ray radiation facilities under proposal number A20-1-864 and we would like to thank for assistance and support in using beamline BM20. The Institute for Beam Physics and Technology at KIT is acknowledged for operation of the KARA and the provision of beamtime at the INE-Beamline, operated by the Institute for Nuclear Waste Disposal at the KIT Light Source. The low temperature heat capacity data reported herein were generated through access to the ActUsLab under the Framework of access to the Joint Research Centre Physical Research Infrastructures of the European Commission (PACIFIED-LFR, FMR/PAMEC access agreement no. 36345/01).

■ REFERENCES

(1) Alencar, L. D.; Mesquita, A.; Feitosa, C. A.; Balzer, R.; Probst, L. F.; Batalha, D. C.; Rosmaninho, M. G.; Fajardo, H. V.; Bernardi, M. I.

Preparation, characterization and catalytic application of Barium molybdate ($BaMoO_4$) and Barium tungstate ($BaWO_4$) in the gas-phase oxidation of toluene. *Ceram. Int.* **2017**, *43*, 4462−4469.

(2) Kowalkinska, M.; Głuchowski, P.; Swebocki, T.; Ossowski, T.; Ostrowski, A.; Bednarski, W.; Karczewski, J.; Zielinska-Jurek, A. Scheelite-type wide-bandgap ABO_4 compounds (A= Ca, Sr, and Ba; B= Mo and W) as potential photocatalysts for water treatment. *J. Phys. Chem. C* **2021**, *125*, 25497−25513.

(3) Ma, X.; Zhao, W.; Wu, J.; Jia, X. Preparation of flower-like $BaMoO_4$ and application in rechargeable lithium and sodium ion batteries. *Mater. Lett.* **2017**, *188*, 248−251.

(4) Smith, A.; Rutten, M.; Herrmann, L.; Epifano, E.; Konings, R.; Colineau, E.; Griveau, J.-C.; Guéneau, C.; Dupin, N. Experimental studies and thermodynamic assessment of the Ba-Mo-O system by the CALPHAD method. *J. Eur. Ceram. Soc.* **2021**, *41*, 3664−3686.

(5) Blasse, G.; Bril, A. On the Eu^{3+} fluorescence in mixed metal oxides. III. Energy transfer in Eu^{3+}-activated tungstates and molybdates of the type Ln_2WO_6 and Ln_2MoO_6. *J. Chem. Phys.* **1966**, *45*, 2350−2355.

(6) Baur, F.; Jüstel, T. Eu^{3+} activated molybdates−Structure property relations. *Opt. Mater.:X* **2019**, *1*, 100015.

(7) van Hattem, A.; Dankelman, R.; Colineau, E.; Griveau, J.-C.; Dardenne, K.; Rothe, J.; Couweleers, S.; Konings, R. J.; Smith, A. L. Experimental investigations and thermodynamic modelling of the ternary system Pb-Mo-O. *J. Alloys Compd.* **2024**, *1003*, 175588.

(8) McMurdie, H. F.; Morris, M. C.; Evans, E. H.; Paretzkin, B.; de Groot, J. H.; Hubbard, C. R.; Carmel, S. J. *Standard X-ray Diffraction Powder Patterns: Section 12−data for 57 Substances*; National Bureau of Standards, 1975; Vol. 25.

(9) Shevchenko, N.; Lykova, L.; Kovba, L. On alkaline earth metal tungstates and molybdates. *Russ. J. Inorg. Chem.* **1974**, *19*, 528−530.

(10) Ryan, R.; Mastin, S.; Reisfeld, M. The crystal structure of $K_2VO_2F_3$, a nonlinear dioxovanadium (V) group. *Acta Crystallogr. Sect. B Struct. Crystallogr. Cryst. Chem.* **1971**, *27*, 1270−1274.

(11) Zavodyannyi, V. V. Refinement of microstructural parameters of the crystal structure of compound Ba_2MoO_5, 2023.

(12) Jantz, S. G.; Pielnhofer, F.; Dialer, M.; Höppe, H. A. On Tungstates of Divalent Cations (I)−Structural Investigation and Spectroscopic Properties of $Sr_2[WO_5]$ and $Ba_2[WO_5]$. *Z. Anorg. Allg. Chem.* **2017**, *643*, 2024−2030.

(13) Scheinost, A. C.; Claussner, J.; Exner, J.; Feig, M.; Findeisen, S.; Hennig, C.; Kvashnina, K. O.; Naudet, D.; Prieur, D.; Rossberg, A.; et al. ROBL-II at ESRF: a synchrotron toolbox for actinide research. *J. Synchrotron Radiat.* **2021**, *28*, 333−349.

(14) Sacristan Civera, A.; Smith, A.; van Hattem, A. Insights into the Chemical Speciation of Chromium Corrosion Products in Molten Salt Fuel Mixtures Using XANES, 2027.

(15) Kieffer, J.; Valls, V.; Blanc, N.; Hennig, C. New tools for calibrating diffraction setups. *J. Synchrotron Radiat.* **2020**, *27*, 558−566.

(16) van Eijck, L.; Cussen, L.; Sykora, G.; Schooneveld, E.; Rhodes, N.; van Well, A.; Pappas, C. Design and performance of a novel neutron powder diffractometer: PEARL at TU Delft. *J. Appl. Crystallogr.* **2016**, *49*, 1398−1401.

(17) Rietveld, H. M. A profile refinement method for nuclear and magnetic structures. *J. Appl. Crystallogr.* **1969**, *2*, 65−71.

(18) van Laar, B.; Schenk, H. The development of powder profile refinement at the Reactor Centre Netherlands at Petten. *Acta Crystallogr., Sect. A:Found. Adv.* **2018**, *74*, 88−92.

(19) Rodríguez-Carvajal, J. Recent advances in magnetic structure determination by neutron powder diffraction. *Phys. B* **1993**, *192*, 55−69.

(20) Momma, K.; Izumi, F. VESTA 3 for three-dimensional visualization of crystal, volumetric and morphology data. *J. Appl. Crystallogr.* **2011**, *44*, 1272−1276.

(21) Rothe, J.; Butorin, S.; Dardenne, K.; Denecke, M.; Kienzler, B.; Löble, M.; Metz, V.; Seibert, A.; Steppert, M.; Vitova, T.; et al. The INE-Beamline for actinide science at ANKA. *Rev. Sci. Instrum.* **2012**, *83*, 043105.

(22) Ravel, B.; Newville, M. ATHENA ARTEMIS, HEPHAESTUS: data analysis for X-ray absorption spectroscopy using IFEFFIT. *J. Synchrotron Radiat.* **2005**, *12*, 537−541.

(23) Bunău, O.; Joly, Y. Self-consistent aspects of x-ray absorption calculations. *J. Phys.: Condens. Matter* **2009**, *21*, 345501.

(24) Guda, S. A.; Guda, A. A.; Soldatov, M. A.; Lomachenko, K. A.; Bugaev, A. L.; Lamberti, C.; Gawelda, W.; Bressler, C.; Smolentsev, G.; Soldatov, A. V.; et al. Optimized Finite Difference Method for the Full-Potential XANES Simulations: Application to Molecular Adsorption Geometries in MOFs and Metal−Ligand Intersystem Crossing Transients. *J. Chem. Theory Comput.* **2015**, *11*, 4512−4521.

(25) Javorský, P.; Wastin, F.; Colineau, E.; Rebizant, J.; Boulet, P.; Stewart, G. Low-temperature heat capacity measurements on encapsulated transuranium samples. *J. Nucl. Mater.* **2005**, *344*, 50−55.

(26) Shannon, R. D. Revised effective ionic radii and systematic studies of interatomic distances in halides and chalcogenides. *Acta Crystallogr. Sect. A Cryst. Phys. Diffr. Theor. Gen. Crystallogr.* **1976**, *32*, 751−767.

(27) Kools, F.; Koster, A.; Rieck, G. The structures of potassium, rubidium and caesium molybdate and tungstate. *Acta Crystallogr. Sect. B Struct. Crystallogr. Cryst. Chem.* **1970**, *26*, 1974−1977.

(28) Brown, I.; Shannon, R. Empirical bond-strength−bond-length curves for oxides. *Acta Crystallogr. Sect. A Cryst. Phys. Diffr. Theor. Gen. Crystallogr.* **1973**, *29*, 266−282.

(29) Yamamoto, T. Assignment of pre-edge peaks in K-edge x-ray absorption spectra of 3d transition metal compounds: electric dipole or quadrupole? *X Ray Spectrom.* **2008**, *37*, 572−584.

(30) van Hattem, A.; Vlieland, J.; Dankelman, R.; Thijs, M. A.; Wallez, G.; Dardenne, K.; Rothe, J.; Konings, R. J.; Smith, A. L. Structural Studies and Thermal Analysis in the Cs_2MoO_4-$PbMoO_4$ System with Elucidation of β-$Cs_2Pb(MoO_4)_2$. *Inorg. Chem.* **2023**, *62*, 6981−6992.

(31) Glasser, L. Additive single atom values for thermodynamics I: Volumes, entropies, heat capacities of ionic solids. *J. Chem. Thermodyn.* **2022**, *166*, 106685.

(32) Cordfunke, E. H. P.; van der Laan, R.; van Miltenburg, J. Thermophysical and thermochemical properties of BaO and SrO from 5 to 1000 K. *J. Phys. Chem. Solids* **1994**, *55*, 77−84.

(33) Gurvich, L.; Polyshchuk, V.; Yorish, V.; Yungman, V. The IVTAN Data Bank on the Thermodynamic Properties of Individual Substances. *Data for Science and Technology*; Springer, 1981; pp 371, 373.